



## Study of contact resistance at the electrode–interconnect interfaces in planar type Solid Oxide Fuel Cells

Tapobrata Dey<sup>a</sup>, Debanand Singdeo<sup>a</sup>, Manaswita Bose<sup>a</sup>, Rajendra N. Basu<sup>b</sup>, Prakash C. Ghosh<sup>a,\*</sup>

<sup>a</sup> Department of Energy Science and Engineering, Indian Institute of Technology Bombay, Mumbai 400076, India

<sup>b</sup> Fuel Cell and Battery Division, CSIR-Central Glass and Ceramic Research Institute, Kolkata 700032, India

### H I G H L I G H T S

- Theoretical and experimental study of contact resistance in SOFCs is carried out.
- Model capable of predicting contact resistance based on statistical surface parameters.
- A minimum load of 0.064 MPa is recommended for minimum contact resistance values.
- Contact resistance for cathodic/anodic interface is 33.3/48 mΩ cm<sup>2</sup> at 0.064 MPa.
- Anodic/cathodic contact resistance increases/decreases with rise in temperature.

### A R T I C L E I N F O

#### Article history:

Received 15 November 2012

Received in revised form

14 January 2013

Accepted 16 January 2013

Available online 28 January 2013

#### Keywords:

Solid Oxide Fuel Cells

Contact resistance

Modeling

Stacking load

### A B S T R A C T

Ohmic resistance at the interface of the electrode and the interconnect in Fuel Cells influences the overall performance of a cell. In the present work, contact resistances between interconnect and electrodes in planar type Solid Oxide Fuel Cells (SOFC) under various compression loads and at different temperatures are measured in laboratory scale experiments. The roughness of the electrode and interconnect surfaces is characterized and a mathematical model to determine the contact resistance at the interfaces with known morphology, is proposed. The experimental results are found to be in good agreement with the values obtained from the model.

© 2013 Elsevier B.V. All rights reserved.

## 1. Introduction

Fuel cell technology is considered to be one of the prospective options for power generation in the present era of energy crisis and security [1]. Among various types of fuel cells, Solid Oxide Fuel Cell (SOFC) is considered to be one of the promising alternatives for power generation because of its high power density and efficiency when operated in combined heat and power (CHP) mode [2]. Moreover, high operating temperatures (650–1000 °C) of SOFCs make it simpler while using hydrocarbon based fuels. In SOFC, a ceramic electrolyte is placed between two porous electrodes, which are further sandwiched between a pair of bipolar plates that act as housing of the cell. Performance of a single SOFC has been the focus of research during the last decade [3]. Researchers

have focused on increasing the power density by developing electrodes as well as electrolyte materials and improving their preparation techniques. Suresh et al. have presented a detailed discussion on various methodologies including tape casting, screen printing, wet powder spraying, colloidal deposition and aerosol jet<sup>®</sup> printing explored for preparation of electrolyte and electrodes used in SOFC [4]. With the recent advancement in the material science, it is now, possible to achieve a power density as high as 2.45 W cm<sup>−2</sup> [5] in the laboratory scale SOFC, however, it is observed that the performance decreases drastically with the increase in the active area of the cell [6–8]. One of the reasons behind the loss in performance of large cells, is identified to be a sharp increase in the contact resistance which is attributed to non-optimal contact between the electrode and the interconnect [8–10]. Each of the engaging surfaces has a roughness which results in an actual contact area smaller than the apparent size of the cell. The Ohmic resistance is inversely proportional to the actual contact area which essentially indicates that an increase in the

\* Corresponding author. Tel.: +91 22 2576 7896; fax: +91 22 2576 4890.  
E-mail addresses: [pcghosh@iitb.ac.in](mailto:pcghosh@iitb.ac.in), [chhamugram@gmail.com](mailto:chhamugram@gmail.com) (P.C. Ghosh).

**Nomenclature**

$A_C$	actual contact area (cm <sup>2</sup> )
$A_O$	apparent contact area (cm <sup>2</sup> )
$A_{CR}$	critical area (cm <sup>2</sup> )
$\alpha$	bandwidth parameter
$B$	constant
$C$	constant
$\delta$	compression of asperities (μm)
$d$	interplanar spacing (μm)
$d^*$	dimensionless interplanar spacing
$d_{CR}$	critical interplanar spacing (μm)
$D_{sum}$	density of summits (μ m <sup>-2</sup> )
$E_{eq}$	equivalent Young's modulus (GPa)
$E_i$	Young's modulus of $i$ -th material (GPa)
$F$	force (N)
$f(z)$	distribution function for asperity heights
$m_i$	spectral moment
$n$	integral power
$\sigma_{sum}$	standard deviation of summits (μm)
$P$	pressure (MPa)
$P_{CR}$	critical pressure (MPa)
$R_C$	radius of contact (μm)
$R_{CR}$	critical contact radius (μm)

$R_{Con}$	resistance due to contact between the electrode and interconnect (mΩ)
$R_{El}$	bulk resistance of the electrode (mΩ)
$R_{IC}$	interconnect resistance (mΩ)
$R_m$	mean asperity radius (μm)
$R_m^*$	dimensionless mean asperity radius
$R_{Total}$	total resistance (mΩ)
$R_{Con}^{ASR}$	area specific contact resistance (mΩ cm <sup>2</sup> )
$\rho_i$	bulk resistivity (Ω cm)
$S_Y$	yield strength (Pa)
$U(x,t)$	parabolic cylindrical function
$\nu_i$	Poisson's ratio of $i$ -th material
$z$	asperity height (μm)
$z^*$	non-dimensional asperity height
$z_{CR}$	critical asperity height (μm)
$\xi$	regime parameter

**Abbreviations**

CHP	combined heat and power
LSM	Lanthanum Strontium Manganite
MEK	Methyl Ethyl Ketone
SOFC	Solid Oxide Fuel Cell
YSZ	Yttria stabilized zirconia

contact at the interface, leads to lower resistive loss. The interfacial contact between the electrode and the interconnect can be improved by applying external load. On the other hand, an excessive load may damage the cell. It is thus, of importance to develop a model that can relate the contact resistance and the applied load for any surface morphology, so that the adequate clamping pressure required to minimize the resistive loss, can be estimated a priori. To the best of the authors' knowledge, no mathematical model to predict the contact resistance in an SOFC under a certain applied load is available in open domain literature, however, a few articles [11–20] have investigated the effect of contact resistance on the performance of PEMFC using numerical as well as experimental techniques. In the present study, efforts have been made to estimate the area specific resistance between the electrodes and the interconnect of an SOFC under various external loads. The influence of the surface morphology on the loading condition in SOFC has also been addressed in the current work.

Every surface possess irregularities at the microscopic level although they may appear to be smooth at the macroscopic scale. The tip of the surface irregularity is termed as asperity. The asperities are of different shapes such as spherical, hemi-spherical and conical [21]. These asperities interact when two surfaces come into contact and play crucial role in determining the behavior of the interface under any applied load [22]. Early work on interaction between surfaces under external load, dates back to 1882 when Hertz proposed his theory on elasticity and laid the foundation of contact mechanics. The subject has since then been enriched by the contribution from several researchers and models for plastic and elasto-plastic deformations for rough surfaces have been developed [23–29]. Greenwood et al. have developed a model where they have assumed a distribution of the surface asperities and determined the elastic deformation at the interface [25]. At a later date, Nayak et al. have proposed a scheme through which the distribution of the asperities can be characterized [30] and the elastic deformation of a surface with known morphology under load can be predicted.

In the present work, the roughness of the anode, cathode and interconnect are determined using surface profilometry. The data is

analyzed and the distribution of asperity heights are obtained. The surface parameters obtained from the experiments are introduced in the model along with the material properties to determine the variation of contact resistance with compression load. The influence of temperature on resistance is investigated in the study. The outcome of the model is validated against the results obtained from the experiments.

**2. Experimental methodology**

Anode and cathode of dimension 1 cm × 1 cm, are prepared using the technique described in the following sections. The electrodes and the interconnects together are placed under varying load and the resistance is measured. The detailed experimental procedure is described subsequently.

**2.1. Anode sample preparation**

The anode electrode is fabricated by tape casting technique. Initially, mixture of nickel oxide (NiO) and Yttria-stabilized zirconia (YSZ) powder is ball milled in an azeotropic mixture of toluene and ethanol to prepare the slurry. Subsequently, the slurry is further ball milled in presence of optimized amounts of organic binder, plasticizer and graphite porosifier. The resultant slurry is then uniformly spread using doctor's blade to form a single green sheet of NiO–YSZ. These green sheets of NiO–YSZ are cut into desired size (12 cm × 12 cm), and multiple cutout sheets are laminated at room temperature to achieve a thickness of ~1.5 mm. The green block of NiO–YSZ is fired at around 1250 °C for around 5–6 h followed by binder burning at 1400 °C to obtain the ultimate sintered anode. Finally, anode samples with dimensions 1 cm × 1 cm are carved out from 10 cm × 10 cm anode sheets.

**2.2. Cathode sample preparation**

Cathode material is prepared using Lanthanum Strontium Manganite (LSM) powder through combustion technique [31,32]. A precursor solution containing La(NO<sub>3</sub>)<sub>3</sub>·6H<sub>2</sub>O (Sisco Research

Laboratory, India),  $\text{Sr}(\text{NO}_3)_2$  (S. D. fine Chemicals, India) and  $\text{Mn}(\text{CH}_3\text{COO})_2 \cdot 4\text{H}_2\text{O}$  (Merck, India) is combined in proper ratio with  $\text{C}_3\text{H}_4\text{OH}(\text{COOH})_3 \cdot \text{H}_2\text{O}$  (Merck, India) and sprayed into the reaction chamber of an in-house built spray pyrolyser at about  $300^\circ\text{C}$  to obtain  $\text{La}_{0.65}\text{Sr}_{0.3}\text{MnO}_3$ . The spray mist undergoes a controlled oxidation–reduction reaction leading to the formation of an ash precursor. Thereafter, the sample is calcinated at  $1000^\circ\text{C}$  resulting in phase pure oxide with optimized particle size. Subsequently, LSM powder is mixed using required quantity of Methyl Ethyl Ketone (MEK) binder and porosifier with agate motel pastel to from a palette of 20 mm diameter at around  $3\text{ N m}^{-2}$  pressure. The plates are further sintered at about  $1200^\circ\text{C}$ . The LSM powder is added with required organic vehicle for the screen printing application. These LSM plate samples are screen-printed with the same material. It is important to note that the process is being adopted because the stack is also screen-printed using the same technique. The sample is fired at  $1000^\circ\text{C}$  and finally the cathode sample is prepared.

### 2.3. Contact resistance measurement

Four probe technique is employed to measure the contact resistance between the electrode interconnect interface. The benefit of this technique is that even small resistances can be measured without any significant errors. The setup consists of an interconnect and electrode samples of dimension  $1\text{ cm} \times 1\text{ cm}$ , placed facing each other. On both the sides, very fine platinum meshes are used for the electrical contact. A pair of contact is fabricated on both the platinum meshes such that they are located diagonally opposite to each other. Finally, the whole arrangement is placed between a pair of alumina plates which helps in insulating the sample. The bottom alumina plate also acts as support for the assembly and loads are applied on the top plate to achieve requisite pressure at the interfaces. The complete arrangement is supplied with constant current from a current source with tolerance  $\pm 2\%$ . The potential differences across the sides are measured using high precession multimeter. Measured potential difference includes the contribution of the resistance due to bulk material used for interconnect and electrode as well as the contact resistance as shown in Fig. 1. The total resistance  $R_{\text{Total}}$  at the interfaces can be expressed as,

$$R_{\text{Total}} = R_{\text{El}} + R_{\text{Con}} + R_{\text{IC}} \quad (1)$$

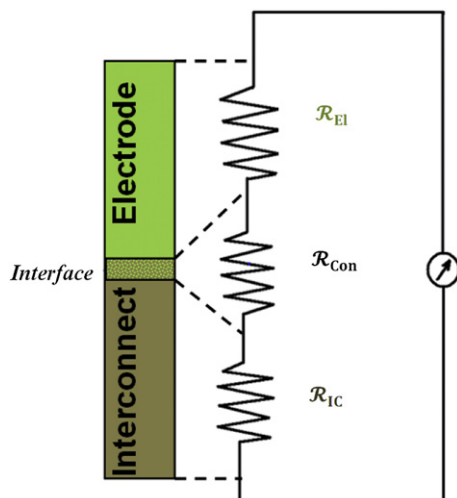


Fig. 1. Equivalent electrical circuit of an electrode interconnect assembly.

where,  $R_{\text{El}}$  and  $R_{\text{IC}}$  are the bulk resistance of the electrode and interconnect respectively.  $R_{\text{Con}}$  represents the contact resistance between the electrode and interconnect. In order to determine the voltage drop arising from the bulk resistance of the electrode and interconnect, individual components are connected to the current source and corresponding voltage drops are noted. Finally, the voltage drop due to material components is subtracted from the total to obtain the contact resistance at different pressures and temperatures.

#### 2.3.1. Cathode–interconnect interface

Since, the cathode electrode deals with the oxygen/air, the experimental setup does not require any isolation from the atmosphere for measuring the contact resistances at the electrode and interconnect interfaces. The measurement setup used for the cathode side is shown in Fig. 2. The assembled cathode–interconnect assembly along with a given compression load is placed inside a furnace and the measurements are recorded at different temperatures.

#### 2.3.2. Anode–interconnect interface

Unlike cathode, the anode electrode of SOFC is sensitive to presence of air as it forms non-conducting oxide at the interfaces. As a preventive measure, a special experimental arrangement is fabricated to provide hydrogen atmosphere in the experimental chamber. The anode electrode and the interconnect assembly is mounted inside a metal chamber as shown in Fig. 3 and placed in the furnace. The metal chamber is perfectly sealed on the base plate using sealant to eliminate the presence of air. The metallic chamber consists of one inlet and one outlet along with a pressure gauge on the inlet side to control the pressure within the chamber. Initially, air is evacuated from the chamber and the anode which is in an oxide form is reduced with hydrogen. After reduction, the voltage drop across the sample is measured at different temperatures under different compression load. To investigate the variation in contact resistance with the compression load, the breakage of sealant is required at every step to alter the applied load.

## 3. Experimental results

In present study, the contact resistances on the anode side as well as cathode side of SOFC are measured as a function of temperature as well as compression load. The variation in the contact resistances between the interconnect and anode at different temperatures are presented in Fig. 4. Initially, the contact resistance diminishes sharply with the increase in the compression load, however, the decrease becomes insignificant when the load reaches a certain threshold value. This occurs at an approximate compression load of  $0.074\text{ MPa}$  and the contact resistance observed in this case is  $48\text{ m}\Omega\text{ cm}^2$  when the operating temperature is maintained at  $800^\circ\text{C}$ . Since, both the surfaces engaged at the interface are metallic in nature, the contact resistance increases with the increase in operating temperature. The contact resistance at the saturation region undergoes an increase from  $40\text{ m}\Omega\text{ cm}^2$  to  $48\text{ m}\Omega\text{ cm}^2$  when the operating temperature is increased from  $600^\circ\text{C}$  to  $800^\circ\text{C}$ .

The variation in the contact resistances between the cathode and interconnect at different temperature and load is presented in Fig. 5. The variations in contact resistance on the cathode side exhibit similar trend as that on the anode side, however, unlike anode side, it is observed that the contact resistances on cathode side decrease with the increase in the operating temperatures. This is due to the electrical properties of the materials engaged at the interfaces. Although the interconnect holds metallic properties the cathode material possess semiconductor properties. The resistance

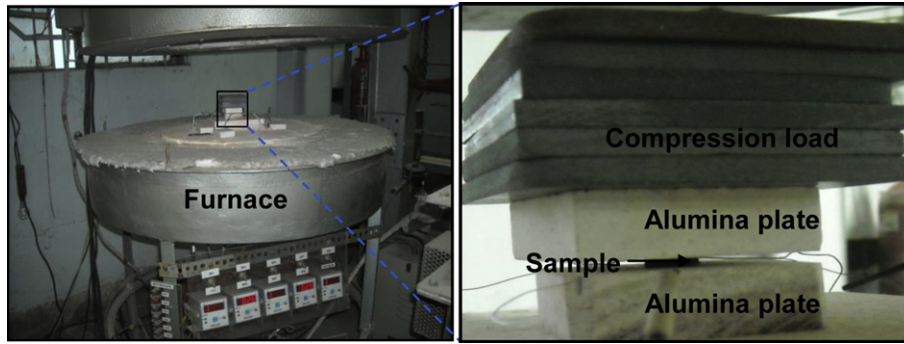


Fig. 2. Experimental arrangement for measuring contact resistance on cathode side.

arises from the cathode dominates at the interface compared to the interconnect leading to higher contact resistance compared to the anode side. Since, the resistivity of the semiconductor decreases with the increase in temperature, the contact resistance on the cathode side decreases with the increase in temperature.

From the graph it is evident that, the contact resistance decreases sharply as load increases and nearly saturates at a compression load of 0.064 MPa when it is kept at 800 °C which indicates that a compression load of 0.064 MPa is needed to achieve minimum contact resistance at the cathode–interconnect interface. The corresponding resistance at this load is observed as 33 mΩ cm<sup>2</sup> at 800 °C.

#### 4. Modeling of contact resistances

A mathematical model based on the theory of deformation of rough surface, is developed to determine the Ohmic resistance at the interface under compression load. The microscopic morphology of the electrodes and the interconnects are determined using surface profilometry and is introduced in the model. A typical microscopic morphology of anode surface is shown in Fig. 6.

Following assumptions are made for modeling the contact in case of SOFC interconnect–electrode interface:

- The asperity heights follow normal distribution.
- The deformation of one asperity does not influence the deformation of others.
- The asperity possesses spherical summits.

The detailed model is described in the next sections.

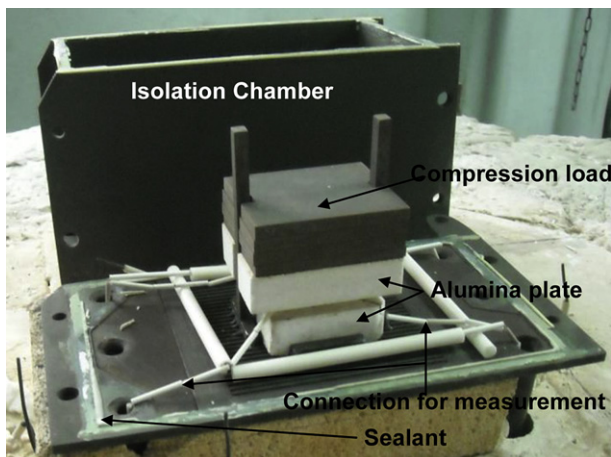


Fig. 3. Experimental setup for measuring the contact resistance on the anode side.

#### 4.1. Elastic contact model

Contact force required to produce deformation of an asperity in contact with a plane is related to its deformation, the radius of curvature of asperity summit and equivalent Young's modulus [23] according to the following equation:

$$F(z) = \frac{4}{3} E_{eq} R_m^{\frac{1}{2}} (z - d)^{\frac{3}{2}} \quad (2)$$

where,  $F(z)$  is the force,  $z$  denotes the asperity height and  $d$  is the inter-planar spacing as described in Fig. 7. The constant  $E_{eq}$  is the effective Young's modulus for the surfaces in contact and is defined as,

$$E_{eq} = \left( \frac{1 - \nu_1^2}{E_1} + \frac{1 - \nu_2^2}{E_2} \right)^{-1} \quad (3)$$

where,  $\nu_1, \nu_2$  are the Poisson's ratio and  $E_1, E_2$  are the Young's modulus of the respective materials for the two surfaces.

The contact radius for a single asperity  $R_C$  is a function of the summit radius  $R_m$  of the asperity, the height of the asperity  $z$  and the inter-planar spacing  $d$ , (Fig. 8) and is expressed as,

$$R_C = \sqrt{R_m(z - d)} \quad (4)$$

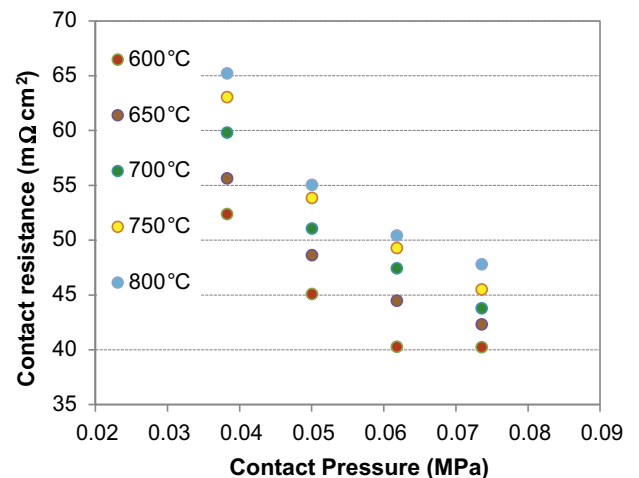


Fig. 4. Variation in contact resistance between anode and interconnect at different temperatures.

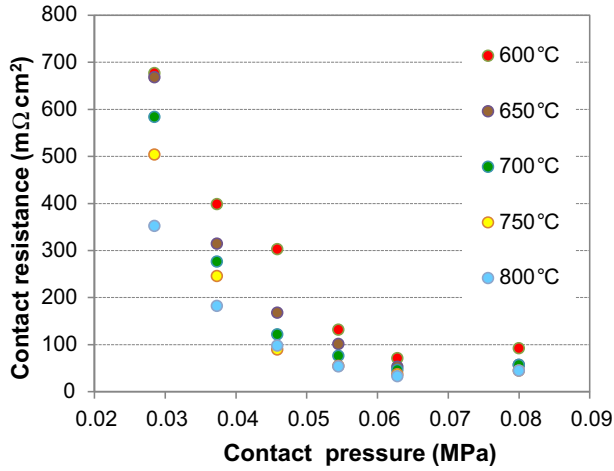


Fig. 5. Variation in contact resistance between cathode and interconnect at different temperatures.

The classical theory of Holm allows the calculation of resistance  $\mathcal{R}_{\text{Con}}$  for a flat circular contact area of a known contact radius [33]. The contact resistance can be estimated at the interface using the following relation:

$$\mathcal{R}_{\text{Con}} = \left( \frac{\rho_1 + \rho_2}{4R_c} \right) \quad (5)$$

where,  $\rho_1$  and  $\rho_2$  are the bulk resistivity of the materials present at the interface.

The introduction of dimensionless quantities is found effective in reducing the complexity of the calculations. They are obtained by dividing quantities  $z$ ,  $d$  and  $R_m$ , having the dimension of length by the standard deviation of summit heights,  $\sigma_{\text{sum}}$ .

Henceforth, dimensionless variables  $z^*$ ,  $d^*$  and  $R_m^*$  will be used to denote asperity height, interplanar separation and radius of curvature of summit. The functional relations for contact force and resistance given in Equations (2) and (5) can be expressed using dimensionless quantities as follows:

$$F(z^*) = \frac{4}{3} E_{\text{eq}} (R_m^*)^{\frac{1}{2}} (z^* - d^*)^{\frac{3}{2}} \sigma_{\text{sum}}^2 \quad (6)$$

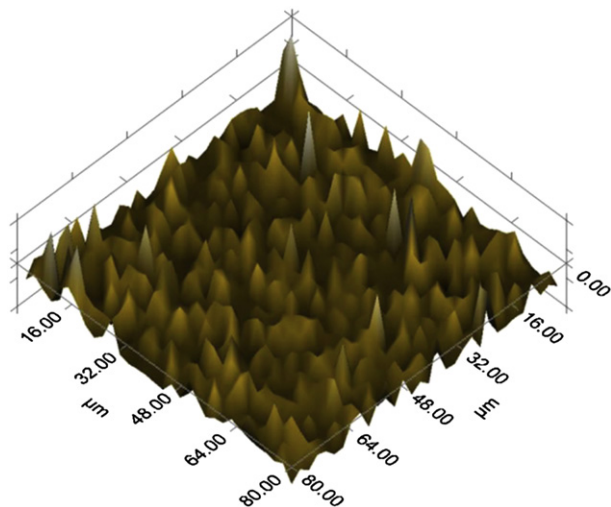


Fig. 6. Microscopic surface morphology of an apparently smooth SOFC anode.

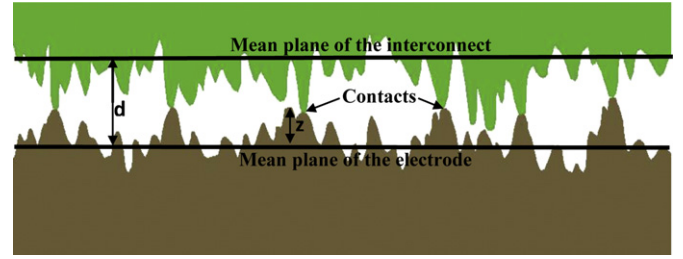


Fig. 7. Illustration of contact mechanism between a pair of rough surfaces.

$$\mathcal{R}_{\text{Con}}(z^*) = \frac{\rho_1 + \rho_2}{4(R_m^*)^{\frac{1}{2}} (z^* - d^*)^{\frac{1}{2}} \sigma_{\text{sum}}} \quad (7)$$

The formulation for a pair of contacts can be extended to the entire interface by considering distribution of the asperity heights. The summit mean plane, also used as reference for a pair of rough surfaces is situated at a certain height above the mean plane of the surface. The number of asperities that make contact when the two surfaces approach each other can be predicted once the separation between the mean planes is determined. Any asperity that will possess height greater than the separation will participate in the contact phenomena. It is observed that the summit heights generally follow Gaussian or Normal distribution [34]. In dimensionless form, Normal distribution can be represented as,

$$f(z^*) = \frac{1}{\sqrt{2\pi}} e^{\left( \frac{-z^{*2}}{2} \right)}. \quad (8)$$

It is not physically possible for asperities located below the mean plane of the surface to participate in the contact phenomenon. The number of contacts actively engaged at the interface, can be determined by integrating the function  $f(z^*)$  over all asperity heights greater than the separation between the mean planes of the surfaces. As a result, contact force can be evaluated from the following integral:

$$F(d^*) = A_0 \int_{d^*}^{\infty} D_{\text{sum}} F(z^*) f(z^*) dz^* \quad \text{For } z^* > d^* \quad (9)$$

where,  $A_0$  represents the nominal surface area.

In order to relate the contact force generated at the interface to the applied load, it is necessary to quantify the actual total area of contact  $A_c$ . This is related to the nominal contact area  $A_0$  given in Equation (9),

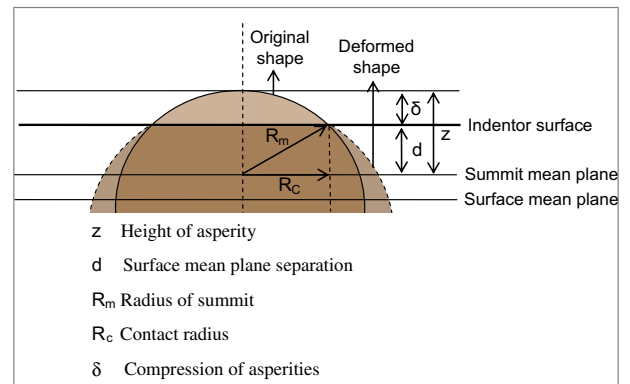


Fig. 8. Contact geometry of a single summit on a rough surface with a smooth surface.

$$A_C(d^*) = A_0 \int_{d^*}^{\infty} \pi R_m^* D_{\text{sum}} (z^* - d^*) \sigma_{\text{sum}}^2 f(z^*) dz^*. \quad (10)$$

The corresponding applied load is given by,

$$P(d^*) = \frac{F(d^*)}{A_C}. \quad (11)$$

Similarly, the corresponding values of contact resistance are calculated for the same interplanar separation using,

$$\mathcal{R}_{\text{Con}}^{\text{ASR}}(d^*) = \int_{d^*}^{\infty} \frac{\mathcal{R}_{\text{Con}}(z^*) f(z^*) dz^*}{D_{\text{sum}}}. \quad (12)$$

One of the methods to evaluate the integral is by expressing it in terms of parabolic cylindrical functions [35] given by,

$$\int_{d^*}^{\infty} (z^* - d^*)^n f(z^*) dz^* = F_n(d^*) \quad (13)$$

$$F_n(d^*) = \frac{n!}{\sqrt{2\pi}} \frac{U\left(n + \frac{1}{2}, d^*\right)}{e^{\frac{d^{*2}}{4}}}. \quad (14)$$

In the current work, the parabolic cylindrical functions have been evaluated using commercial software MAPLE (version 7).

The parameters  $\sigma_{\text{sum}}$ ,  $R_m$  and  $D_{\text{sum}}$  can be calculated from the surface spectral moments.

The slope and curvature of the profile can be computed by employing four point finite central difference schemes to the filtered data from the profilometer [36]. The moments in that case calculated from their respective expectation values are written below [37].

$$m_0 = E(z^2) \quad (15)$$

$$m_2 = E\left(\left\{\frac{dz}{dx}\right\}^2\right) \quad (16)$$

$$m_4 = E\left(\left\{\frac{d^2z}{dx^2}\right\}^2\right) \quad (17)$$

The bandwidth parameter  $\alpha$  can be estimated from the following equation:

$$\alpha = \frac{m_0 m_4}{m_2^2}. \quad (18)$$

The density of summits  $D_{\text{sum}}$  is estimated from the second and fourth moment as,

$$D_{\text{sum}} = \frac{1}{6\pi\sqrt{3}} \left(\frac{m_4}{m_2}\right). \quad (19)$$

Similarly the radius of contact area,  $R_m$  and standard deviation of summit,  $\sigma_{\text{sum}}$  is calculated from fourth moment and bandwidth parameter using Equations (20) and (21) respectively.

$$R_m = \frac{3}{8} \left(\frac{\pi}{m_4}\right)^{\frac{1}{2}} \quad (20)$$

$$\sigma_{\text{sum}} = \left[ \left(1 - \frac{0.8968}{\alpha}\right) m_0 \right]^{\frac{1}{2}} \quad (21)$$

Considering the surfaces to be isotropic in nature, the interface will possess spectral moment equivalent to the sum of respective surface moments [38].

$$m_{ie} = m_{ix} + m_{iy}, \quad \text{where } i = 0, 2, 4. \quad (22)$$

#### 4.2. Plastic contact model

For the elastoplastic model, the approach lay down by Jackson and Green [26] is followed. The transition from elastic to plastic deformation domain occurs when the applied load exceeds the critical pressure for the corresponding asperity. The expression for the critical pressure is given as Ref. [26]:

$$P_{\text{CR}} = \frac{4}{3A_{\text{CR}}} \left(\frac{R_m}{E_{\text{eq}}}\right)^2 \left(\frac{\pi C S_Y}{2}\right)^3 \quad (23)$$

where,  $S_Y$  is the yield strength of the material being indented. The parameter  $C$  can be estimated from the Poisson's ratio as,

$$C = 1.295 \exp(0.736\nu) \quad (24)$$

At critical pressure, the area of contact (critical area), is determined from,

$$A_{\text{CR}} = \pi^3 \left(\frac{R_m C S_Y}{2E_{\text{eq}}}\right)^2 \quad (25)$$

If the asperities are compressed beyond a critical value, the deformation occurs in elastoplastic regime. The critical interference parameter also allows the prediction of the transition from elastic to plastic behavior,

$$\psi_s = \sqrt{\frac{\sigma_{\text{sum}}}{z_{\text{CR}} - d_{\text{CR}}}} \quad (26)$$

$$z_{\text{CR}} - d_{\text{CR}} = R_m \left(\frac{\pi C S_Y}{2E_{\text{eq}}}\right)^2 \quad (27)$$

and

$$B = 0.14 \exp\left(23 \left(\frac{S_Y}{E_{\text{eq}}}\right)\right) \quad (28)$$

The general relation of contact area of a single asperity is related with deformation in the form of Equation (29).

$$R_{\text{CR}} = \sqrt{\xi R_m (z - d)} \quad (29)$$

$$\xi = 1, \quad \text{if } 0 \leq \left(\frac{z - d}{z_{\text{CR}} - d_{\text{CR}}}\right) \leq 1.9 \quad (30)$$

$$\text{and } \xi = \left(\frac{z - d}{z_{\text{CR}} - d_{\text{CR}}}\right)^B, \quad \text{if } \frac{z - d}{z_{\text{CR}} - d_{\text{CR}}} \geq 1.9 \quad (31)$$

#### 4.3. Estimation of contact resistances

For present investigation, NiO–YSZ, LSM and ferritic steel (Crofer 22 APU) are considered respectively as anode, cathode and interconnect materials. The surface morphologies of all the above mentioned components acquired using profilometer (XP2 Stylus) are shown in Fig. 9. The properties essential for estimating the electrical contact resistance obtained from the individual surface

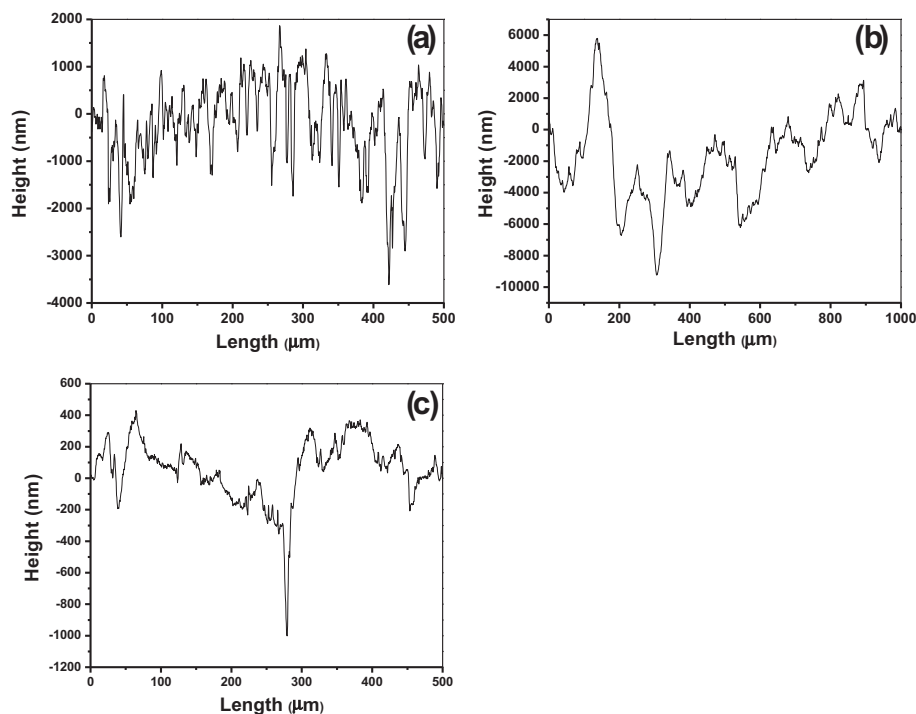


Fig. 9. Surface profile obtained from profilometer (a) anode (b) cathode and (c) interconnect.

morphology are summarized in Table 1. Other important physical properties required for the estimation of the contact resistances are summarized in Table 2.

The parameters mentioned in Table 1 provide information about the nature of the two interfaces. The band-width parameter  $\alpha$  for the anode–interconnect interface has a value of around 68, which is quite less compared to the cathode–interconnect interface. There is also less deviation in the heights of the asperities. The standard deviation of peak heights is around two times greater for the cathode surface. This can also be related to the profilometer images which clearly show that the magnitude of asperity heights exist within a narrow range in case of anode. These factors show that the anode–interconnect interface has less roughness compared to the cathode–interconnect. Moreover, it is of interest to note that the summit density is higher in case of the anode–steel interface. A higher summit density can yield more contact spots when the plane of separation is reduced under the action of force.

#### 4.4. Results from contact models

The interface contact model is used for prediction of the contact resistance under the application of a load across  $1 \text{ cm}^2$  mating surfaces. The Young's modulus of both the anode and cathode values are obtained from experiments using nano-indentation

technique and these values are used within the framework of the model. The applied load is computed by choosing appropriate values for the interplanar spacing. The same values of interplanar spacing are used in the model to estimate the contact resistance. Contact resistance between anode and interconnect estimated from the elastic model is shown along with the experimental data in Fig. 10. A good agreement between the experimental results with the modeling is observed. With the aid of model it can be reasoned that only a few asperities are in contact at the interface at low loads. This translates into higher values for contact resistance. As load is increased successively, more deformation of the asperities in contact occurs and the interplanar spacing is reduced further. At this reduced separation more asperities now come in contact, increasing the total contact area. The rapid increase in contact area between the asperities leads to dramatic fall in resistance values. Further increase in load does not offer significant improvement in the contact resistances.

The elastoplastic contact model has been used in case of the cathode–interconnect interface for studying the change in contact resistance under applied load at different temperatures. The yield strength for the cathode material is 0.6 GPa. The plasticity index for the cathode material is found to be 42 using Equation (26) which is quite high. A high value of plasticity index indicates that the asperities for the surface under consideration would possibly undergo plastic deformation. Contact resistance between cathode and

Table 1  
Surface parameters obtained from surface profile.

Parameters	Anode–steel	Cathode–steel
$D_{\text{sum}} (\mu \text{ m}^{-2})$	0.064	0.028
$\sigma_{\text{sum}} (\mu \text{ m})$	1.22	2.68
$R_m (\mu \text{ m})$	2.13	7.56
$\alpha$	68.13	766.53

Table 2  
Important physical properties of anode cathode and interconnect.

Component	Materials	Properties at 800 °C	
		Resistivity ( $\text{m}\Omega \text{ cm}$ )	Young's modulus (GPa)
Anode	Ni–YSZ	2.22	41
Cathode	LSM	10.0	22
Interconnect	Crofer 22 APU	0.1	44 [39]

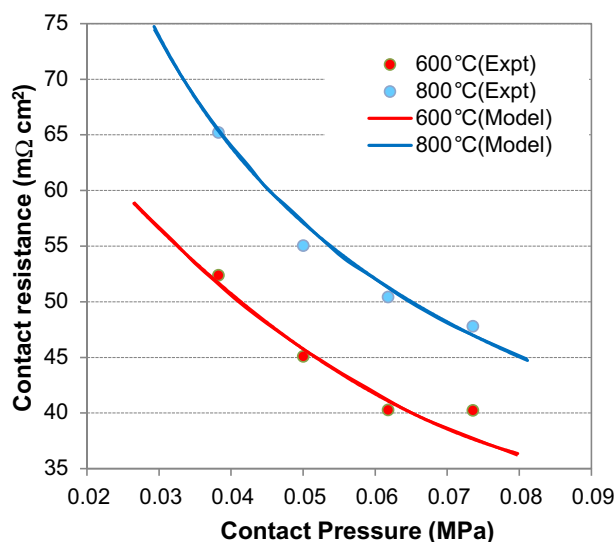


Fig. 10. Validation of anode and bi-polar plate contact resistance at 600 °C and 800 °C.

interconnect estimated from the elastoplastic model is shown along with the experimental data in Fig. 11. It is clear that the modeling results follow experimental trend. The variation in the contact resistance is found to be high in case of the cathode compared to the anode. The summit density for cathode is less as seen from surface profile data and therefore, the numbers of contact points are few in contrast with anode at a particular load. This is one of the causes leading to the observation of higher resistance values at the cathode interconnect interface. The experimental results indicate a sharp drop in contact resistance when load is varied from 0.025 MPa to 0.045 MPa. This is the region of transition of elastoplastic contact. Finally beyond 0.05 MPa at 800 °C the deformation is entirely plastic. The resistance value in the plastic contact region is found to vary slightly between 45 mΩ cm<sup>2</sup> and 52 mΩ cm<sup>2</sup>. Further increase in load offers no significant improvement in the values of contact resistance.

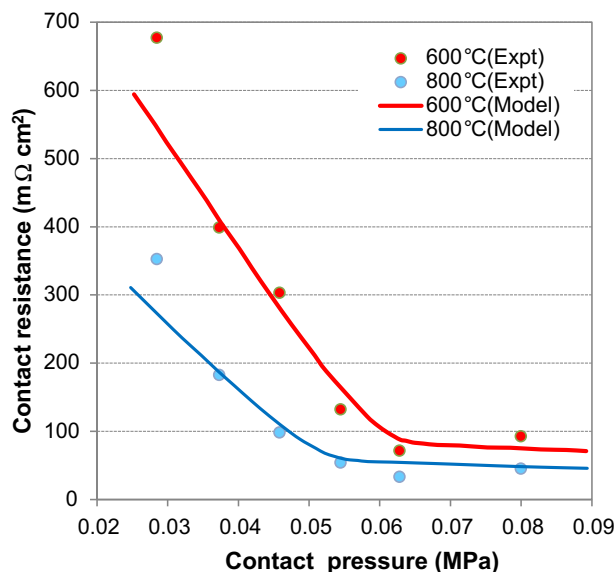


Fig. 11. Variation of cathode–interconnect contact resistance with load at 600 °C and 800 °C.

## 5. Conclusions

In this paper, Ohmic resistance at the contact between the electrode–interconnect interfaces in planar type SOFCs is measured. A model to determine the interfacial contact resistance for any engaging surfaces with known morphology is proposed. The results obtained from the model are compared with the experimental observation. The experiments are carried out in the temperature range of 600 °C–800 °C. Since, the cathode possess the characteristics of semiconductor, the contact resistance on the cathode side decreases with the increase in temperature. Conversely, the contact resistance on the anode side increases with the increase in operating temperatures. It is observed that the contact resistance reaches low values at a compression load of 0.064 MPa. For cathode–interconnect interface the corresponding resistance obtained is 33.3 mΩ cm<sup>2</sup> at 800 °C. Further increase in load causes marginal variations in the contact resistances. In case of the anode–interconnect interface under a compression load of 0.074 MPa, the contact resistance is found to be 48 mΩ cm<sup>2</sup> at 800 °C. Results indicates that optimum compression load for achieving minimum contact resistance lies in the range of 0.064–0.074 MPa. The modeling results are found to be in good agreement with the experimental results. The modeling results suggest that the cathode undergoes a transition from elastic to plastic and an elastoplastic model is necessary to predict the variation in contact resistances. The elastic model is able to explain the variations in the contact resistances with compression pressure in the ranges 0.03–0.075 MPa on the anode side.

## Acknowledgments

The authors (TD and RNB) express their sincere gratitude to Director, CGCRI for giving permission to publish this work. One of the authors (TD) gratefully acknowledges financial support received from Council of Scientific and Industrial Research for Senior Research Fellowship.

## References

- [1] M. Barber, T.S. Sun, E. Petrach, X. Wang, Q. Zou, J. Power Sources 185 (2008) 1252–1256.
- [2] S.C. Singhal, K. Kendall, High Temperature Solid Oxide Fuel Cells: Fundamentals, Design and Applications, first ed., Elsevier, Amsterdam, 2003, pp. 53–80.
- [3] R.N. Basu, A. Das Sharma, A. Dutta, J. Mukhopadhyay, Int. J. Hydrogen Energy 33 (20) (2008) 5748–5754.
- [4] A.M. Sureshini, F. Meisenkothen, P. Gardner, T.L. Reitz, J. Power Sources 224 (2013) 295–303.
- [5] M. Mukhopadhyay, J. Mukhopadhyay, A. Das Sharma, R.N. Basu, Int. J. Hydrogen Energy 37 (2012) 2524–2534.
- [6] P.C. Ghosh, T. Wüster, H. Dohle, N. Kimiaie, J. Mergel, D. Stolten, J. Fuel Cell Sci. Technol. 3 (2006) 351–357.
- [7] H. Dohle, J. Mergel, P.C. Ghosh, Electrochim. Acta 52 (2007) 6060–6067.
- [8] T. Dey, P.C. Ghosh, D. Singdeo, M. Bose, R.N. Basu, Int. J. Hydrogen Energy 36 (16) (2011) 9967–9976.
- [9] P. Zhou, P. Lin, C.W. Wu, Z. Li, Int. J. Hydrogen Energy 36 (2011) 6039–6044.
- [10] S.P. Jiang, J.G. Love, L. Apateanu, Solid State Ionics 160 (2003) 15–26.
- [11] X.Q. Xing, K.W. Lum, H.J. Poh, Y.L. Wu, J. Power Sources 195 (2010) 62–68.
- [12] J. Tan, Y.J. Chao, J.W. Van Zee, W.K. Lee, Mater. Sci. Eng. A 445–446 (2007) 669–675.
- [13] J. Ihonen, F. Jaouen, G. Lindbergh, G. Sundholm, Electrochim. Acta 46 (2001) 2899–2911.
- [14] X. Wang, Y. Song, B. Zhang, J. Power Sources 179 (2008) 305–309.
- [15] W.R. Chang, J.J. Hwang, F.B. Weng, S.H. Chan, J. Power Sources 166 (2007) 149–154.
- [16] P. Zhou, C.W. Wu, G.J. Ma, J. Power Sources 159 (2006) 1115–1122.
- [17] T. Swamy, E.C. Kumbur, M.M. Mench, Electrochim. Acta 56 (2011) 3060–3070.
- [18] V. Mishra, F. Yang, R. Pitchumani, J. Fuel Cell Sci. Technol. 1 (2004) 2–9.
- [19] D. Liu, L. Peng, X. Lai, J. Power Sources 195 (2010) 4213–4221.

- [20] F. Tietz, H.P. Buchkmmmer, V.A.C. Haanappel, A. Mai, N.H. Menzler, J. Mertens, W.J. Quadakkers, D. Rutenbeck, S. Uhlenbruck, M. Zahid, D. Stöver, *Ceram. Eng. Sci. Proc.* 25 (3) (2004) 269–274.
- [21] A.R. Sohoul, A.M. Goudarzi, R.A. Alashti, *J. Surf. Eng. Mater. Adv. Technol.* 1 (2011) 125–129.
- [22] I.J. Ford, *J. Phys. D: Appl. Phys.* 26 (1993) 2219–2225.
- [23] H. Hertz, *Miscellaneous Papers*, Macmillan and Co Ltd, New York, 1986, pp. 146–162.
- [24] D.J. Whitehouse, J.F. Archard, *Proc. R. Soc. London, Ser. A* 316 (1970) 97–121.
- [25] J.A. Greenwood, J.B.P. Williamson, *Proc. R. Soc. London, Ser. A* 295 (1442) (1966) 300–319.
- [26] R.L. Jackson, I. Green, *Tribol. Int.* 39 (2006) 906–914.
- [27] A.W. Bush, R.D. Gibson, P. Keogh, *Wear* 35 (1) (1975) 87–111.
- [28] R.L. Jackson, J.L. Streater, *Wear* 11–12 (2006) 1337–1347.
- [29] H. Zahouani, R. Vargiolu, J.L. Loubet, 28 (4–8) (1998) 517–534.
- [30] P.R. Nayak, *J. Lubr. Technol., Trans. ASME* 93 (3) (1971) 398–407.
- [31] M.W. Raja, S. Mahanty, P. Ghosh, R.N. Basu, H.S. Maiti, *Mater. Res. Bull.* 42 (2007) 1499–1506.
- [32] B.P. Mandal, A. Dutta, S.K. Deshpande, R.N. Basu, A.K. Tyagi, *J. Mater. Res.* 24 (9) (2009) 2855–2862.
- [33] R. Holm, *Electric Contacts: Theory and Application*, Springer, New York, 1967, pp. 9–16.
- [34] B. Bhushan, *Introduction to Tribology*, John Wiley and Sons, New York, 2002, pp. 17–18.
- [35] T. Swamy, E.C. Kumbur, M.M. Mench, *J. Electrochem. Soc.* 157 (1) (2010) B77–B85.
- [36] D. Dowson, *Tribological Research and Design for Engineering Systems*, Elsevier, Amsterdam, 2003, p. 207.
- [37] J.I. McCool, *Wear* 107 (1986) 37–60.
- [38] T. McWaid, E. Marschall, *Int. J. Heat Mass Transfer* 35 (11) (1992) 2911–2920.
- [39] Y.T. Chiu, C.-K. Lin, J.C. Wu, *J. Power Sources* 196 (2011) 2005–2012.